Article

Antimicrobial Properties of MgO Nanostructures on Magnesium Substrates

Jiajia Lin, Nhu-Y Thi Nguyen, Chaoxing Zhang, Alexandra Ha, and Huinan Hannah Liu*

Read Online

ACCESS | Metrics & More | Article Recommendations

ABSTRACT: Magnesium (Mg) and its alloys have attracted increasing attention in recent years as medical implants for repairing musculoskeletal injuries because of their promising mechanical and biological properties. However, rapid degradation of Mg and its alloys in physiological fluids limited their clinical translation because the accumulation of hydrogen (H_2) gas and fast release of OH^- ions could adversely affect the healing process. Moreover, infection is a major concern for internally implanted devices because it could lead to biofilm formation, prevent host cell attachment on the implants, and interfere osseointegration, resulting in implant failure or other complications. Fabricating nanostructured magnesium oxide (MgO) on magnesium (Mg) substrates is promising in addressing both problems because it could slow down the degradation process and improve the antimicrobial activity. In this study, nanostructured MgO layers were created on Mg substrates using two different surface treatment techniques, i.e., anodization and electrophoretic deposition (EPD), and cultured with *Staphylococcus aureus* in vitro to determine their antimicrobial properties. At the end of the 24-h bacterial culture, the nanostructured MgO layers on Mg prepared by anodization or EPD both showed significant bactericidal effect against *S. aureus*. Thus, nanostructured MgO layers on Mg are promising for reducing implant-related infections and complications and should be further explored for clinical translation toward antimicrobial biodegradable implants.
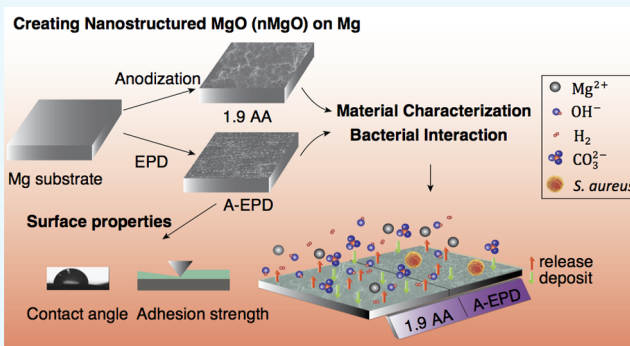
1. INTRODUCTION

In recent years, Mg and Mg alloys as bioresorbable metals have attracted increasing attention for orthopedic implant applications due to their promising mechanical and biological properties.[1] Mg is biocompatible and biodegradable.[2] Unlike conventional nondegradable metals, Mg-based implants do not require secondary surgeries for implant removal.[2,3] Mg and Mg alloys have higher elastic modulus and strength than biodegradable polymers and better fracture toughness than ceramics, which are more desirable for load-bearing implants.[2,4−7] Mg has a similar modulus to human bone and thus reduces the undesirable stress-shielding effect on the surrounding bone,[3,8,9] which is beneficial for bone health. Recent advances in biodegradable Mg have demonstrated their potential for revolutionizing the treatments for bone fractures.[10−12] The screws made of high-purity Mg (99.99 wt % pure) have demonstrated better fracture healing and proper degradation rate when compared with the poly-L-lactide acid (PLLA) screws in the fixation of rabbit femoral intercondylar fractures.[13] The high-purity Mg screws also showed acceptable mechanical strength and degradation rates compatible with bone formation for the fixation of femoral neck fractures in goats.[14] Furthermore, the high-purity Mg was studied clinically to fix the vascularized bone grafts for human patients with

osteonecrosis of the femoral head (ONFH) and showed a higher Harris hip score (HHS) when compared with the controls using vascularized bone grafting alone without screws.[15] However, it is difficult and expensive to produce Mg of super high purity (>99.9 wt %).[16] The small amount of impurity in commercially 99−99.9 wt % pure Mg matrix could lead to rapid degradation and release of excessive hydrogen gas at the early stage of implantation.[1,17,18] A previous study showed that the gas cavities induced subcutaneous emphysema and decreased the survival rate of rats, which remained as the key challenge for clinical translation of Mg-based biometals.[19]

Either adding alloying elements into the Mg matrix or applying surface treatment on Mg or both are promising approaches to improve the overall performance of Mg-based biometals for clinical applications. For example, the Mg−Ca−Zn alloy screws showed acceptable degradation in the fixation
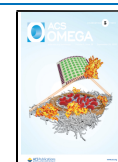
of hand fractures in clinical studies, and the alloy screws were completely replaced by new bone within 1 year of implantation and the patients regained a normal range of grip power.[20] Rare earth (RE) elements have also been added to Mg to reduce the corrosion rate. Mg−RE alloy screws showed proper degradation and osseointegration in treating the patients with mild hallux valgus when compared with the titanium (Ti) screw control.[10] Surface treatment of Mg and Mg alloys has also been explored to further improve their corrosion resistance and surface bioactivity for tissue healing[16,21] and even provide antimicrobial properties to reduce infection.

Clinically, implant-associated infections have caused devastating complications, with a reported occurrence rate of 2−5% on average.[22,23] *Staphylococcus aureus* and *Staphylococcus epidermidis* are the major bacteria that account for 70% of orthopedic implant infections.[24−26] These bacteria could adhere onto implant surfaces, proliferate, and form protective polymeric biofilms that are more difficult to eradicate than planktonic bacteria in the body, even with the treatment of antibiotics. The reason is that biofilms facilitate the resistance against host defense mechanisms and confer antibiotic resistance because of the slow transportation of antibiotics through the biofilm matrix.[27−29] Moreover, the formation of biofilms on the implants could prevent the attachment of host cells on the implant surface, leading to poor osseointegration and implant failure.[30,31] The biofilm dispersal at the late stage of biofilm formation could lead to detachment and spreading of bacteria, causing systemic infections should the bacteria reach the bloodstream.[31−34] Therefore, preventing implant infections is crucial for improving clinical outcome.

One approach to increase the corrosion resistance of Mg-based metals and disrupt bacterial adhesion is to modify the surface, including surface chemistry and topography. Magnesium oxide (MgO) nanoparticles showed antimicrobial properties against both Gram-negative and Gram-positive bacteria in vitro, including *Escherichia coli* and *Staphylococcus aureus*[35−38] We found that MgO nanoparticles interact with the Gram-negative and Gram-positive bacteria differently.[38] Specifically, the minimum inhibitory concentration (MIC) of MgO nanoparticles was lower for Gram-positive bacteria, that is, 0.5 mg/mL for *S. epidermidis* and 0.7 mg/mL for *S. aureus*, but higher for Gram-negative bacteria, that is, 1 mg/mL for *E. coli* and *Pseudomonas aeruginosa*.[38] Moreover, when the Gram-negative bacteria were cultured with MgO nanoparticles of greater than 1.6 mg/mL, no viable *E. coli* and less than 0.1% *P. aeruginosa* were found. In the cases of Gram-positive bacteria, MgO nanoparticles of up to 2.0 mg/mL only showed inhibitory effects on the growth of *S. epidermidis* and *S. aureus*, but did not kill the bacteria completely. Importantly, when MgO nanoparticles were coated onto poly-ʟ-lactic acid (PLLA), the samples showed antimicrobial properties against *S. aureus*, *S. epidermidis*, and *P. aeruginosa* in vitro.[39] In terms of the responses from relevant host cells, MgO nanoparticles with a low dosage of less than 200 μg/mL could enhance the proliferation of bone-marrow-derived mesenchymal stem cells (BMSCs) under in vitro sequential seeding culture,[37] which is beneficial for bone regeneration. MgO nanoparticles coated onto poly(methyl methacrylate) (PMMA) and poly-ʟ-lactic acid (PLLA) showed enhanced osteoblast and fibroblast adhesion under in vitro culture.[39,40] In addition to these desirable bioactivities, applying a dense MgO layer onto Mg substrates could reduce Mg degradation in the physiological environment.[41,42] Mg and its alloys suffer rapid corrosion in humid air (65% relative humidity) and form white, flaky corrosion products of magnesium hydroxide and magnesium oxide.[43−45] However, the natural oxide layers on the surface of Mg are neither as stable nor as protective as the oxide layers that typically form on the aluminum and titanium alloys.[46] The natural oxide layers formed on Mg are loose and easy to break away, which could accelerate the degradation of Mg. The thickness of these naturally formed oxide layers on Mg is usually in the nanometer scale.[47,48]

Anodization and electrophoretic deposition (EPD) techniques have been previously established for creating dense MgO nanostructures on Mg substrates under controllable processing parameters.[41,42] Both anodization and EPD are cost-effective and versatile for producing protective oxide layers with adjustable thickness and surface morphology on various metallic substrates by adjusting the voltage/current, anodization/deposition time, and electrolyte properties (compositions, concentrations, pH, etc.).[41,42,49,50] Other methods such as alkaline treatment and plasma electrolytic oxidation (PEO) could also be used to create a layer of MgO or $Mg(OH)_2$ on Mg. However, surface oxide layers prepared with alkaline treatment are not compact and dense, and the PEO process typically requires high voltage that could create minipores in the oxide layers. In both cases, aggressive ions, proteins, and cells in the physiological environment could attack the material surface and jeopardize the corrosion resistance of Mg-based substrates.[51−54] In contrast, dense and compact oxide layers have been created on Mg in our previous studies using anodization and EPD methods with optimized processing parameters of electrolyte compositions, concentrations, and anodization/deposition time.[41,50,55,56] The MgO nanostructures on Mg substrates reduced hydrogen (H_2) gas formation during degradation and showed no adverse effect on bone-marrow-derived mesenchymal stem cells (BMSCs) in vitro under the indirect contact conditions of direct culture.[41,42] However, the antimicrobial properties of nanostructured MgO on Mg substrates for medical applications have not been investigated. Therefore, the objectives of this study were to investigate and compare the microstructures, elemental compositions, surface, and interfacial properties of the nanostructured MgO on Mg substrates prepared by anodization versus EPD, and determine their antimicrobial properties against *S. aureus* using a method adapted from the Japanese Industrial Standard JIS Z 2801:2000 (as shown in Figure 1),[57] and the correlation between the processing, surface properties, and the bactericidal effects of the nanostructured MgO layers on Mg substrates. In this study, commercially pure Mg (99.9 wt%) was used as an underlying substrate for developing nanostructured oxide layers using both anodization and EPD methods to exclude the variability induced by different alloying elements. For example, Mg−Zn−Ca alloys showed greater inhibitory effects on bacterial growth when compared with commercially pure Mg control,[58] which would induce additional factors affecting bacterial responses. Therefore, commercially pure Mg instead of Mg alloys was used as the substrate in this study to focus on the effects of the nanostructured MgO surface on bacterial interaction.

2. RESULTS

2.1. Surface Microstructures and Elemental Compositions.
Figure 2 shows the surface characterization for the samples prepared by anodization before annealing (labeled as 1.9 A), by anodization after annealing (labeled as 1.9 AA), by
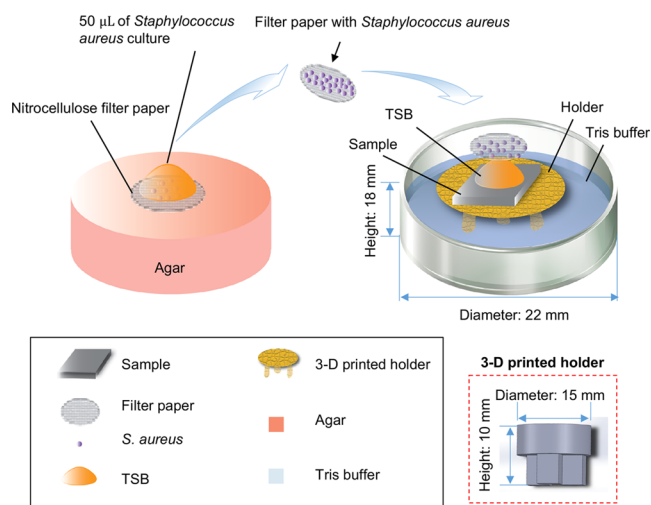
Figure 1. Schematic illustration of the methods used to study the antimicrobial properties of the Mg-based samples. The red dashed square at the right corner highlights the three-dimensional (3D) printed sample holder and its dimensions. The nitrocellulose filter paper had a diameter to be the same as the width of the samples and fit on top of the square-shaped sample as an inscribed circle to ensure all of the bacteria will be in contact with the sample surface.

EPD before annealing (labeled as EPD), and by EPD after annealing (labeled as A-EPD). The images from scanning electron microscopy (SEM) in Figure 2a at the original magnifications of 150× (first column), 10 000× (second column), and 40 000× (inset in the second column) show the representative nano-to-micron surface features for each sample. The overlay of SEM images and energy-dispersive X-ray spectroscopy (EDS) maps at an original magnification of 150× are shown in the third column. The SEM images at a low magnification of 150× confirmed the homogeneous surface morphology of the 1.9 A sample. At a high magnification of 40 000, the nanoscale crystal structure was observed in the anodized layer of the 1.9 A sample. After annealing, microcracks appeared on the 1.9 AA sample, with the crack width of 0.19 ± 0.15 μm based on the measurement for the SEM images taken at an original magnification of 10 000×.

The SEM images at a low magnification of 150× confirmed the homogeneous surface morphology of the EPD sample. At a high magnification of 40 000×, nanoscale particles were observed in the coating layer of the EPD sample. After annealing, the SEM images of the A-EPD sample at 150× show that the MgO nanoparticles tended to fuse along the polishing line on Mg and the size of the particles became larger when compared with that before annealing (EPD). The high-magnification SEM image shows that the nMgO coating became more compact and dense after the annealing process (A-EPD) when compared with the coating surface before annealing (EPD).

The overlaid SEM images and EDS maps in the third column in Figure 2a show the homogeneous elemental distribution of Mg and O. The EDS results are shown in Figure 2b. The atomic ratio of O/Mg for the 1.9 A sample is 1.9, which indicated that the composition of the anodized Mg sample is $Mg(OH)_2$. The EDS results of the 1.9 AA sample show the atomic ratio of 1.2, indicating that $Mg(OH)_2$ converted to MgO after annealing. The EDS results in Figure 2b show the presence of Mg and O elements for the EPD and A-EPD samples; the sample prepared by EPD had a
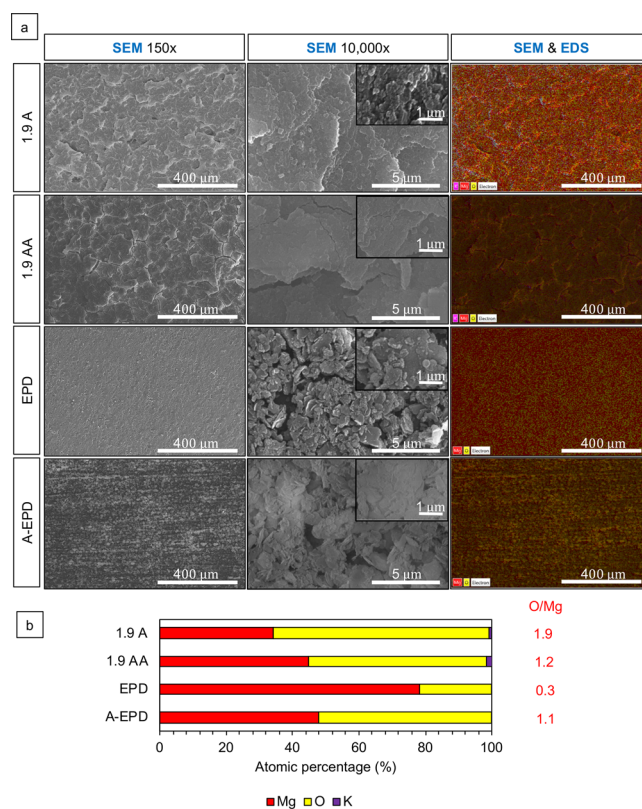

Figure 2. Characterization of the surface microstructure and composition for the surface-treated Mg samples. (a) SEM images of anodized Mg substrates prepared by anodization at 1.9 V vs Ag/AgCl in 10 M KOH at room temperature for 2 h before and after annealing (1.9 A and 1.9 AA, respectively) and nano-MgO (nMgO)-coated Mg substrates prepared by EPD in ethanol at a concentration of 3 mg/mL before and after annealing (EPD and A-EPD, respectively). SEM images were obtained at the original magnifications of 150× (the first column), 10 000× (the second column), and 40 000× (insets in the second column), showing nano-to-micron scale surface micro-structures on each sample. The third column shows the overlaid SEM images and EDS maps at an original magnification of 150×. Scale bar = 400 μm for all SEM images at an original magnification of 150×. Scale bar = 5 μm for all SEM images at an original magnification of 10 000×. Scale bar = 1 μm for all SEM images at an original magnification of 40 000×. (b) Corresponding Atomic percentage (atom %) quantified by EDS area analyses. The EDS analyses were obtained from the SEM images at an original magnification of 150×. The atomic ratio of O/Mg (atom %/atom %) listed next to the EDS graph was calculated based on the corresponding EDS data.

stoichiometric O/Mg atomic ratio of 0.3 before annealing (EPD) and 1.1 after annealing.

2.2. Phase Identification in the Surface-Treated Mg Samples and Mg Control.
The crystalline phases in the surface-treated Mg samples and Mg control were characterized using X-ray diffraction (XRD), as shown in Figure 3. The XRD spectra of the 1.9 A sample show the presence of Mg, MgO, and $Mg(OH)_2$ phases. After annealing, the peak for $Mg(OH)_2$ disappeared and the 1.9 AA sample shows the presence of Mg and MgO in the XRD spectra, which confirmed the dehydration of $Mg(OH)_2$. The XRD spectra of the EPD and A-EPD show the presence of Mg and MgO phases with very small peaks of $Mg(OH)_2$. The XRD spectra of the Mg control show the presence of Mg peaks.
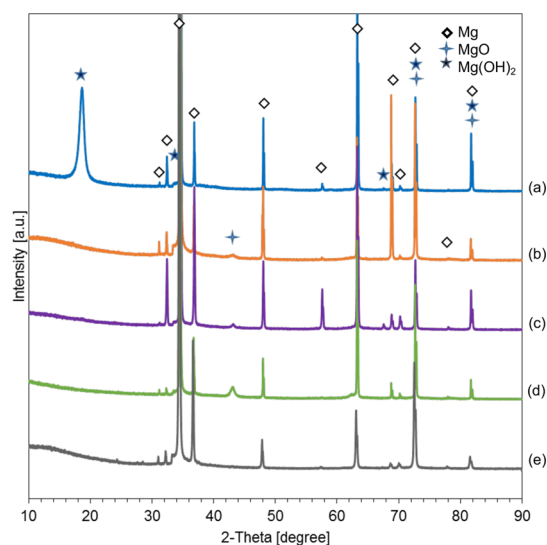
Figure 3. X-ray diffraction (XRD) patterns of the surface-treated Mg samples and Mg control. (a) Anodized Mg (1.9 A); (b) annealed-anodized Mg (1.9 AA); (c) Mg with electrophoretically deposited MgO nanoparticles (EPD); (d) Mg with electrophoretically deposited MgO nanoparticles and annealed (A-EPD); and (e) Mg control. Phases were identified based on Mg (ICSD pattern 01-071-3765), MgO (ICSD pattern 00-030-0794), and $Mg(OH)_2$ (ICSD pattern 00-050-1085) standards.

2.3. Cross-Sectional Analysis of the Samples Prepared by Anodization and EPD.

Figure 4 shows the cross-sectional characterization of the samples of 1.9 A, 1.9 AA, EPD, and A-EPD using SEM and EDS at an original magnification of 2000× and the corresponding EDS maps of elemental distribution for Mg and O. The overlaid SEM images and EDS maps were used to identify the interface between the oxide layers and Mg substrates for measuring the oxide layer thickness. The thicknesses of oxide layers on Mg substrates were 4.1 ± 0.4 and 8.8 ± 1.2 μm for 1.9 A and 1.9 AA, respectively. The surface layers for EPD and A-EPD had thicknesses of 4.4 ± 0.9 and 11.1 ± 0.4 μm, respectively.

2.4. Interfacial Adhesion Strength of the Surface Oxide Layers to Mg Substrates.

Progressive loading from 0 to 150 N was applied on the surface of the samples prepared by anodization (1.9 A and 1.9 AA) over a distance of 2 mm, whereas progressive load from 0 to 3 N was applied on the surface of the samples prepared by EPD (EPD and A-EPD) over a distance of 2 mm, because the interfacial adhesion strengths of the anodized samples (1.9 A and 1.9 AA) are expected to be higher. The loading rate was 5 N/s, and the moving speed was 4 mm/min. Figure 5 shows the normal load and friction force versus the scratch distance. The critical loads L_f at the failure points of the surface layers during the microscratch test are summarized in Table 1. The critical load is the smallest load at which a recognizable failure of the coating occurs. As observed from the microscopic images for all of the samples, the initial mark on the surface layers appeared at the beginning of the test. The failure load of the top layers of the 1.9 A and 1.9 AA was much higher than that of the EPD and A-EPD samples because no delamination occurred between the surface layers and the underlying Mg substrates until the progressive load reached the maximum load of 150 N, as shown in the microscopic images in Figure 5. As the stylus continued to penetrate into the surface layer
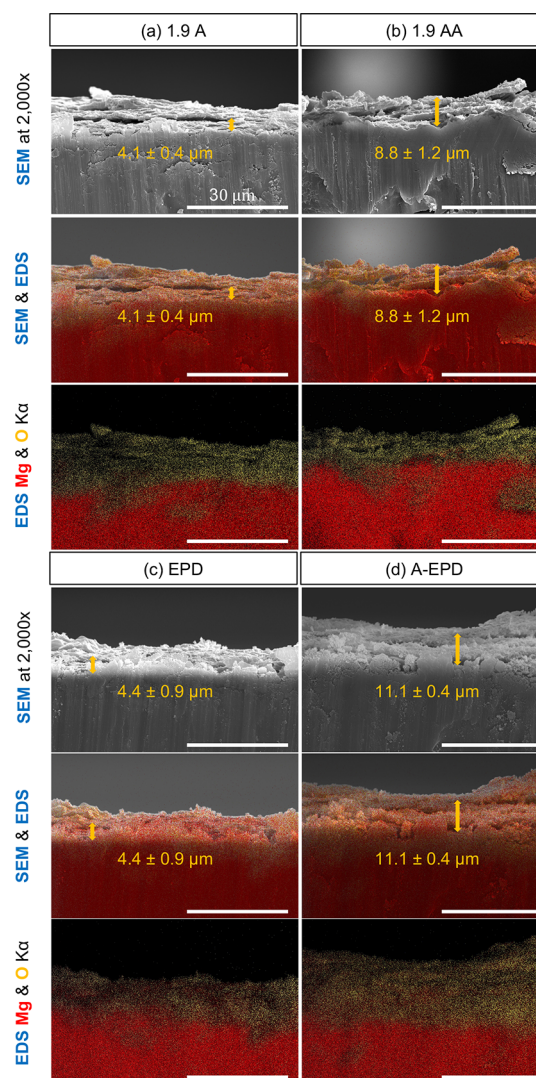

Figure 4. Cross-sectional characterization of the surface-treated Mg samples by SEM and EDS. Montage of SEM images, and overlaid images of SEM and EDS maps of O (yellow), Mg (red), and K (blue), as well as the corresponding overlaid EDS maps (Kα line) for the elemental distribution of O and Mg. (a) Anodized Mg (1.9 A); (b) annealed-anodized Mg (1.9 AA); (c) Mg with electrophoretically deposited MgO nanoparticles (EPD); and (d) Mg with electrophoretically deposited MgO nanoparticles and annealed (A-EPD). SEM images were obtained at an original magnification of 2000×. Scale bar = 30 μm for all SEM images and EDS maps. The average thickness of the oxide layers on Mg substrates was labeled in the SEM images, and overlaid images of SEM and EDS maps of O (yellow), Mg (red), and K (blue), as denoted using the double sided arrows and values of mean ± standard deviation (SD).

prepared by EPD before annealing (EPD), failure of the top layer occurred at 0.55 mm with a load of 0.39 N. For the surface layer prepared by EPD after annealing (A-EPD), failure of the top layer occurred at 0.97 mm with a load of 1.63 N.

2.5. Surface Roughness, Surface Area (SA), and Wettability of the Oxide Layers on Mg Substrates.

Figure 6a−d shows the 3D surface topography, surface roughness, and surface area of the 1.9 A, 1.9 AA, EPD, and A-EPD samples. The respective surface roughness (S_q) of the 1.9 A, 1.9 AA, EPD, and A-EPD samples was 3.7 ± 0.1, 4.3 ± 0.1, 1.2 ± 0.1, and 1.2 ± 0.1 μm. The surface roughness was analyzed using one-way analysis of variance (ANOVA) because
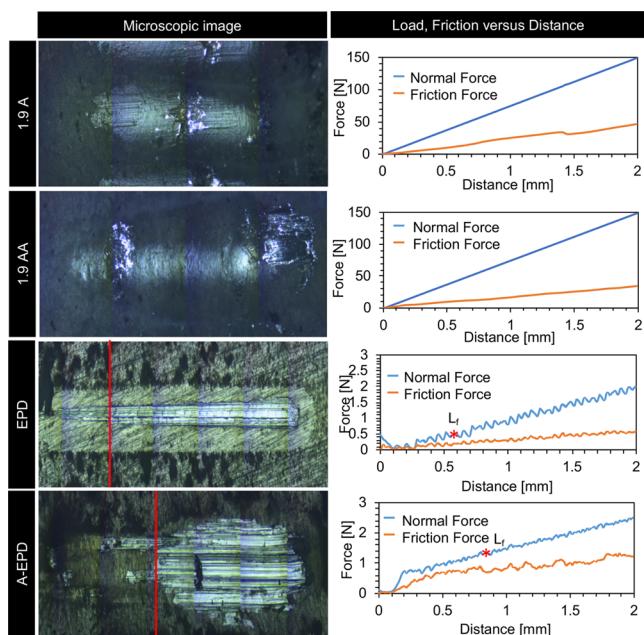
Figure 5. Microscratch testing for interfacial adhesion between the MgO surface layers and Mg substrates. Left column: optical micrographs of the surface after scratch testing. Right column: the results of load, friction force versus distance for the samples of anodized Mg (1.9 A), annealed-anodized Mg (1.9 AA), Mg with electrophoretically deposited MgO nanoparticles (EPD), and Mg with electrophoretically deposited MgO nanoparticles and annealed (A-EPD).

Table 1. Results of Critical Load (L_f) from the Microscratch Testing for the Samples of 1.9 A, 1.9 AA, EPD, and A-EPD

samples	1.9 A	1.9 AA	EPD	A-EPD
L_f [N]	>150	>150	0.17 ± 0.18	1.56 ± 0.07

the data sets were parametric. One-way ANOVA confirmed a significantly higher surface roughness of 1.9 AA sample than that of the 1.9 A sample, but the difference was not considered important because it was so small and around the resolution of the microscope optics. The surface roughness of 1.9 A and 1.9 AA samples was significantly higher than that of the EPD and A-EPD samples. The respective surface areas (SAs) of the 1.9 A, 1.9 AA, EPD, and A-EPD samples were 6.0 ± 0.1, 7.5 ± 0.1, 2.8 ± 0.1, and 2.6 ± 0.2 mm^2, respectively. The surface area was analyzed using one-way ANOVA because the data sets were parametric. One-way ANOVA confirmed a significantly higher surface area of 1.9 AA sample than that of the 1.9 A sample. The surface areas of 1.9 A and 1.9 AA samples were significantly higher than those of the EPD and A-EPD samples.

The surface wettability of each specimen was analyzed using the static contact angle measurements. TSB was used as the liquid droplets on the surface because it was used as culture media for *S. aureus* in the bacterial study. The contact angles of the samples and controls are summarized in Figure 6e, including their corresponding microscopic images acquired during the contact angle measurements. The contact angles of the 1.9 A, 1.9 AA, EPD, A-EPD, Mg, Ti controls, and glass reference were 50.6 ± 1.3, 82.9 ± 3.8, 9.4 ± 3.8, 35.0 ± 3.8, 50.3 ± 5.6, 55.6 ± 3.7, and $52.0 \pm 4.7°$, respectively. The contact angle values were analyzed using one-way ANOVA because the data sets were parametric. The statistical analysis
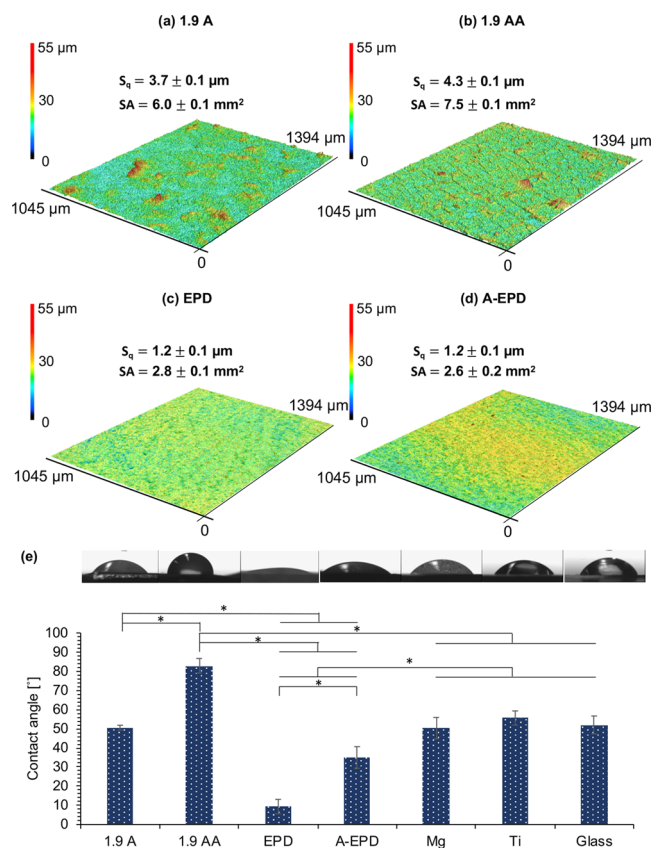

Figure 6. Surface topography, surface roughness, surface area, and contact angle measurements for the surface-treated Mg samples of 1.9 A, 1.9 AA, EPD, and A-EPD. (a–d) Surface topography maps from 3D laser scanning and the calculated surface roughness and surface area for (a) 1.9 A, (b) 1.9 AA, (c) EPD, and (d) A-EPD samples. The scanning area was 1045 μm × 1394 μm. (e) Contact angle measurements for 1.9 A, 1.9 AA, EPD, and A-EPD samples, controls of Mg and Ti, and glass references. Tryptic soy broth (TSB) droplets were used for the contact angle measurements on all samples. The corresponding droplet micrographs were shown on top of the contact angle data. Values are mean ± standard deviation; $n = 3$. *$p < 0.05$.

confirmed that the contact angles of the 1.9 A and 1.9 AA samples were significantly higher than those of the EPD and A-EPD samples. The contact angle of the 1.9 AA sample was significantly higher than that of the 1.9 A sample. The contact angle of the A-EPD sample was significantly higher than that of the EPD sample. The contact angle of the 1.9 AA sample was significantly higher than those of the Mg, Ti controls, and glass reference. The contact angles of the EPD and A-EPD samples were significantly lower than those of the Mg, Ti controls, and glass reference. The contact angles of all of the samples were less than 90°, indicating that the surfaces were hydrophilic.[59]

2.6. Viability of *S. aureus* after 24 h of Culture with the Samples. Bacterial viability was quantified on both the sample surfaces and the filter papers that covered the sample surfaces, by counting the colony forming units (CFUs) on the agar plates, as shown in Figure 7. No viable *S. aureus* was detected on 1.9 A, 1.9 AA, EPD, and their corresponding filter papers, and very few bacteria were found on A-EPD and the corresponding filter paper after 24 h of culture.

For the bacterial viability on the sample surfaces, ANOVA confirmed that the CFUs of *S. aureus* cultured with the 1.9 A and 1.9 AA samples were significantly lower when compared
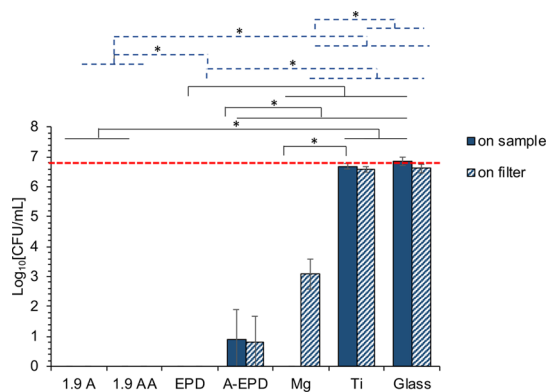
Figure 7. Bacterial density after being cultured in TSB with the surface-treated Mg samples of 1.9 A, 1.9 AA, EPD, and A-EPD, as well as the controls of Mg and Ti, and the glass references for 24 h, as quantified from the colony forming unit (CFU). Bacteria were seeded at an actual concentration of 6×10^6 CFU/mL, as indicated by the red dashed line. The values are the mean $\pm$ standard deviation; $n = 3$. $*p < 0.05$. The black solid line indicated the statistical analysis results for the bacterial density on the sample surfaces. The blue dashed line indicated that the statistical analysis results for the bacterial density on the filters covered the sample surfaces.

with those cultured with Ti control and glass reference. The CFU of *S. aureus* cultured with the EPD sample was significantly lower when compared with those cultured with Mg, Ti controls, and glass reference. The CFU of *S. aureus* cultured with the A-EPD sample was significantly higher when compared with that cultured with the EPD sample, but was significantly lower when compared with those of Mg, Ti controls, and glass reference. ANOVA also confirmed a significantly lower CFU of *S. aureus* for the Mg control when compared with that of the Ti control.

For the viability of bacteria from the filter paper that covered the sample surfaces, ANOVA confirmed a significantly lower CFU of *S. aureus* on the filter paper cultured with the 1.9 A and 1.9 AA samples when compared with that cultured with the A-EPD sample, Mg, Ti controls, and glass reference. The CFU of *S. aureus* on the filter paper cultured with the EPD sample was significantly lower when compared with those of Mg, Ti controls, and glass reference. The CFU of *S. aureus* on the filter paper cultured with the A-EPD sample was significantly higher when compared with that of the EPD sample, but was significantly lower when compared with those of Mg, Ti controls, and glass reference. ANOVA also confirmed a significantly lower CFU of *S. aureus* on the filter paper for the Mg control when compared with those of the Ti control and glass reference.

2.7. Adhesion and Morphology of *S. aureus* after 24 h of Culture with the Samples. SEM images were taken after 24 h of culture with the samples, controls, and references with *S. aureus*, as shown in Figure 8. No *S. aureus* was found on the surfaces of the 1.9 A, 1.9 AA, EPD, and A-EPD samples. Few *S. aureus* was observed on their corresponding filter papers, and the morphology of *S. aureus* on the filter papers that cultured with the 1.9 A, 1.9 AA, EPD, and A-EPD samples was distorted with observable damage in the cell wall and cell membrane, in contrast to the typical round morphology of *S. aureus* as seen in the Ti control and glass reference. The bacteria on the surfaces of the Ti control and glass reference aggregated with an appearance of biofilm, which was also found on their corresponding filter papers. No bacteria were found on the
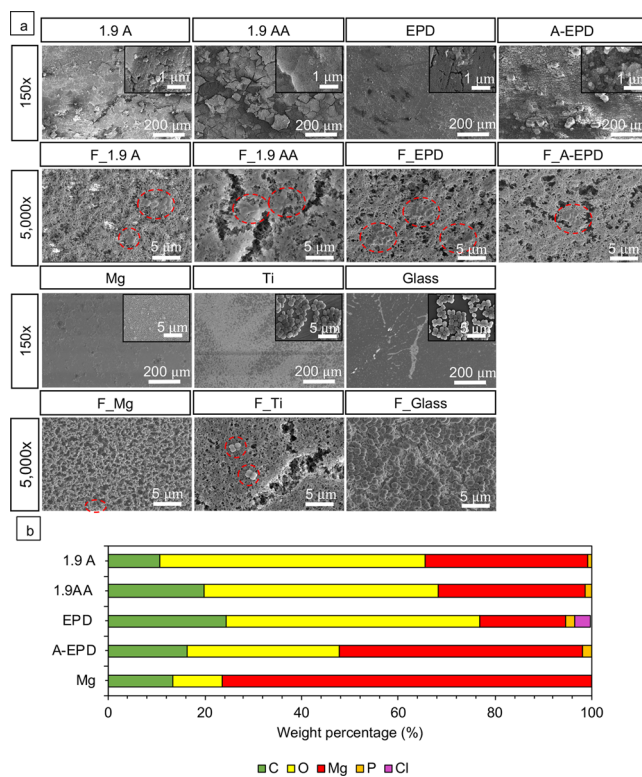

Figure 8. Characterization of the surface microstructure and composition after 24 h of bacterial culture. (a) SEM images of the 1.9 A, 1.9 AA, EPD, A-EPD, Mg, Ti, glass, and the respective nitrocellular filter papers (with F as a prefix in abbreviation) on each sample after bacterial culture. The abbreviations of F_1.9 A, F_1.9 AA, F_EPD, F_A-EPD, F_Mg, F_Ti, and F_Glass refer to the filters on the corresponding samples. SEM images of the samples were obtained at an original magnification of 150× and 40 000× (the inset SEM images), showing nano-to-micron scale surface features for each sample after bacterial culture. SEM images of the respective nitrocellular filter papers were obtained at an original magnification of 5000×. Scale bar = 200 μm for all SEM images at an original magnification of 150×. Scale bar = 5 μm for all SEM images at an original magnification of 5000×. Scale bar = 1 μm for all SEM images at an original magnification of 40 000×. The red dashed circles on the SEM images highlight the adhered *S. aureus* on the surfaces of different samples. Surface elemental compositions (weight %) of the 1.9 A, 1.9 AA, EPD, A-EPD, and Mg samples were quantified by EDS area analyses and plotted in the bar graph. The EDS analyses were performed on the SEM images at an original magnification of 150×.

surface of the Mg control, but some *S. aureus* aggregated on the filter paper that cultured with the Mg control.

The SEM images at an original magnification of 150× and 40 000× (insets) in Figure 8a also show the surface morphology of the samples and controls at the end of the 24-h culture. At a low magnification of 150×, corrosion-induced microcracks propagated along the surfaces of the 1.9 A, 1.9 AA, and A-EPD samples, with crack widths of 1.5 ± 0.6, 2.3 ± 1.1, and 0.4 ± 0.1 μm, respectively, based on the measurements on their responding SEM images at an original magnification of 150×. The surface morphology of the EPD sample was very similar to that of the Mg control, indicating that some MgO coating might have delaminated from the Mg substrate during the bacterial culture. At a high magnification of 40 000×, distinct nanoscale features were observed on the 1.9 A, 1.9 AA, EPD, and A-EPD samples, and corrosion-induced microcracks penetrated through the EPD sample. The

nanostructures of platelet-like morphology were observed on the Mg control at a magnification of 40 000× (inset) and considered to be the $MgO/Mg(OH)_2$ degradation products.

Figure 8b summarizes the elemental composition (in weight %) quantified from the EDS analyses at an original magnification of 150×. Mg, O, C, and P were found on the surfaces of 1.9 A, 1.9 AA, and A-EPD samples after culture with *S. aureus* in TSB. Mg, O, C, P, and trace amount of Cl were found on the surfaces of the samples of EPD after culture with *S. aureus* in TSB. Specifically, the surfaces of the 1.9 AA, EPD, and A-EPD samples had a higher weight percent of C and O when compared with that of the Mg control. In contrast to the surface of the Mg control where only Mg, O, and C elements appeared, the surfaces of 1.9 A, 1.9 AA, EPD, and A-EPD show small amounts of P, indicating phosphorus-containing mineral deposition.

Figure 9 shows the XRD spectra for the 1.9 A, 1.9 AA, EPD, A-EPD samples, and Mg control after a 24-h culture with *S.*
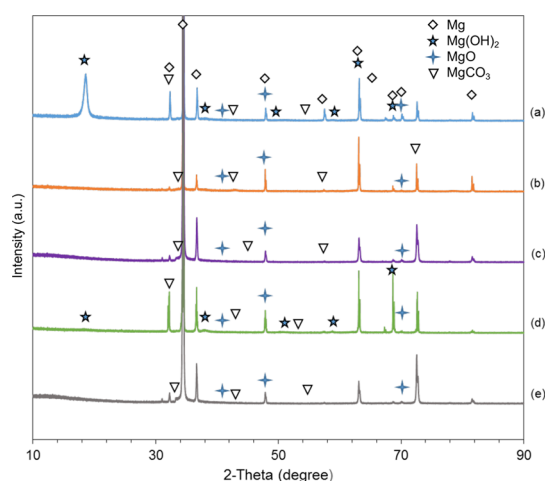

Figure 9. X-ray diffraction patterns of the surface-treated Mg samples and Mg control after a 24-h bacterial culture. (a) Anodized Mg (1.9 A); (b) annealed-anodized Mg (1.9 AA); (c) Mg with electrophoretically deposited MgO nanoparticles (EPD); (d) Mg with electrophoretically deposited MgO nanoparticles and annealed (A-EPD); and (e) Mg. Phases were identified based on Mg (ICSD pattern 01-071-3765), MgO (ICSD pattern 00-030-0794), $Mg(OH)_2$ (ICSD pattern 00-050-1085), and $MgCO_3$ (ICSD pattern 01-086-2348) standards.

aureus in TSB. The phases were identified based on the standards in the Inorganic Crystal Structure Database (ICSD): specifically, 01-071-3765 for Mg, 00-030-0794 for MgO, 00-050-1085 for $Mg(OH)_2$, and 01-086-2348 for $MgCO_3$. The XRD spectra confirmed the newly formed compound $MgCO_3$ and the presence of MgO and $Mg(OH)_2$ on the surfaces of 1.9 A, 1.9 AA, EPD, and A-EPD samples and Mg control, which was in agreement with the EDS analyses. The nanostructured degradation products on the Mg control were most likely to be $MgO/Mg(OH)_2$ considering the platelet-like morphology, as shown in the SEM images in Figure 8, detection of MgO, $Mg(OH)_2$, and $MgCO_3$ phases in the XRD spectra in Figure 9, and other reports in the literature.[41,60,61] In this study, the Mg peaks are much more intense than the other peaks because the surface coating layers were only around a few micrometers, in which the conventional XRD detected the signals from both the coatings and the substrates, producing relatively weak signals from the thin surface layers and intense signals from the

Mg substrates. Similarly, for the thin degradation layers after bacterial culture, the peaks for a phosphorus-containing compound may be too small to be detected, but it was actually in the degradation layers since the presence of P was detected in the EDS results.

3. DISCUSSION

3.1. Comparison of Nanostructured MgO on Mg Prepared by Anodization and EPD.
Different surface treatment techniques could produce surface layers of various thicknesses on Mg substrates with different microstructures, surface properties (i.e., surface roughness, surface area, and surface wettability), and interfacial adhesion strength. Thus, it is essential to compare the oxide layers on Mg substrates prepared using anodization versus EPD for determining the relationships between the processing conditions and the corresponding microstructure, oxide layer thickness, surface properties, and interfacial adhesion strength.

Anodization involves electrochemical reactions to create oxide layers on the surfaces of the working electrodes under certain applied current and voltage.[41] In contrast, during the EPD process, the charged particles suspended in the electrolyte accumulate on the working electrode under the applied electric field, without chemical reactions. Therefore, the characteristics of oxide layers formed on Mg by anodization or EPD would be different. As shown in Figure 2a, a homogeneous, compact $Mg(OH)_2$ layer formed on Mg via anodization, while small pores between particulates were visible on the MgO layer produced by EPD. The surface roughness of the 1.9 AA samples in this study ($S_q = 4.3 \pm 0.1 \ \mu m$) was deemed to be close to the samples in a previous report ($S_q = 3.0 \pm 0.5 \ \mu m$),[41] considering the standard deviation and the resolution of the microscope optics. In comparison with the oxide layers produced by EPD, the surface roughness of oxide layers produced by anodization was significantly higher, likely because of finer $Mg(OH)_2/MgO$ nanostructures of the 1.9 A and 1.9 AA samples, as shown in the SEM images in Figure 2. Rougher surfaces of 1.9 A and 1.9 AA samples exhibited a significantly larger surface area than those of EPD and A-EPD samples. According to the Wenzel model of liquid on solid surfaces, the chemically hydrophilic surface should become more hydrophilic if surface roughness increased.[62] This contradicted our findings on the surface roughness and wettability, likely because of the differences in surface microstructure and elemental composition produced via these two different surface treatment techniques.

After anodization, annealing at 450 °C in argon (Ar) dehydrated the $Mg(OH)_2$ phase and converted the $Mg(OH)_2$ phase into MgO phase, as shown in the XRD spectra in Figure 3. For the specimens prepared by anodization, the change of the Mg/O atomic ratio from 1:1.9 before annealing to 1:1.2 after annealing in Figure 2b, EDS analyses, also supported the chemical conversion of the oxide layers from $Mg(OH)_2$ to MgO through dehydration.[60] The conversion from $Mg(OH)_2$ to MgO during the annealing process resulted in microstructural shrinkage and thus the formation of microcracks throughout the oxide layer, mainly because the decomposition of $Mg(OH)_2$ resulted in the pseudomorphous transformation of each single platelet and the newly formed MgO had a smaller size.[63] In contrast, for the EPD samples, XRD confirmed that the oxide layers were mainly composed of MgO, with a small amount of $Mg(OH)_2$. The atomic ratio between the Mg and O was 1:0.3 before annealing, indicating

that the oxide layer on Mg contained some pores, which allowed the detection of more signals from the underlying Mg substrate. However, the annealing process fused and consolidated the MgO nanoparticles to a dense and compact oxide layer on the Mg substrate (Figure 2), which resulted in an atomic ratio between Mg and O to be 1:1.1, close to 1:1. Even though no significant difference in surface roughness was detected between EPD and A-EPD samples, the oxide layer produced by EPD became less hydrophilic after annealing. Moreover, the annealing process increased the thickness of the oxide layers for the specimens prepared by anodization and EPD: specifically, from 4.1 ± 0.4 μm for 1.9 A to 8.8 ± 1.2 μm for 1.9 AA and from 4.4 ± 0.9 μm for EPD to 11.1 ± 0.4 μm for A-EPD. Cipriano et al.[41] and Cortez Alcaraz et al.[42] reported that the thicknesses for 1.9 A, 1.9 AA, and A-EPD samples were 2.34 ± 0.53, 21.8 ± 8.9, and 10.1 ± 0.3 μm, respectively. The thickness of the oxide layers in this study was considered to be similar to the previous reports within the range of standard deviation.[41,42] In some cases, it was reported that the protection provided by the coating layer was proportional to the coating thickness.[50] In other cases, the corrosion resistance provided by the MgO layers on Mg strongly depended on the combination of surface morphology, surface roughness, surface area, surface wettability, and thickness of MgO.[64,65] Our previous results showed that MgO layers prepared by both anodization and EPD affected the degradation mode and rate of Mg after a 9-day immersion in the revised simulated body fluid (r-SBF) and Dulbecco's modified Eagle's medium (DMEM); that is, such oxide layers resulted in more homogeneous degradation mode and reduced the initial H_2 gas release when compared with noncoated Mg controls.[41,42]

In addition to the surface properties and thickness of the oxide layers, the interfacial adhesion strength between the oxide layer and the underlying Mg substrates is an important parameter to consider for medical implant applications, because any delamination of the surface layers during in vivo implantation could release particulate debris and thus cause adverse effects on the surrounding tissue and implant performance.[66] Clearly, the anodization process could provide superior interfacial adhesion strength between the MgO layers and the underlying Mg substrates due to the presence of chemical bonding at the interface.[67] In this study, the oxide layers created by anodization did not show delamination on the surface even after the microscratch testing at a critical load L_f higher than 150 N. The critical load from the microscratch testing indicates the cohesive (bonding within the coating layers) and adhesive (bonding of a coating to the substrate) strengths of a coating.[68] The higher the critical load, the stronger the interfacial adhesion strength. For the MgO layers on Mg created via anodization, the applied voltage should be lower than the value at which water dissociates, to achieve a compact layer onto Mg. When the anodization voltage is higher than the voltage for water decomposition, oxygen evolution occurs instead of thickening the oxide layers.[6] When the anodization voltage is higher than the dielectric breakdown voltage, usually up to 300 V,[69] or higher up to 500 V,[70] the process is called PEO or microarc oxidation (MAO), where a plasma is generated while the oxide layer grows. The PEO/MAO process would produce craters with sizes of a few microns due to the electric currents locally breaking through the growing layer.[6] Therefore, it is interesting to compare the interfacial adhesion strength of the oxide layers prepared by

different processes, such as MAO/PEO, anodization, and EPD. Durdu et al. developed oxide coatings on Mg using microarc oxidation (MAO) at different current densities, with the critical load ranging from 58 to 84 N when the coating thicknesses ranged from 25 to 40 μm.[71] Aktuğ et al. reported a critical load of 98 and 109 N for the plasma electrolytic oxide (PEO) coatings on the AZ31 Mg alloy in the solution of KOH and two different concentrations of sodium metasilicate pentahydrate ($Na_2SiO_3 \cdot 5H_2O$) electrolytes with the coating thicknesses of 73.3 and 67.6 μm.[72] Mandelli et al. found a critical load from 15 to 22 N for the anodic oxides or oxide/saline composite coatings with or without the addition of nanoparticles (TiO_2, ZrO_2, and Al_2O_3) on the AM60B Mg alloy prepared by microarc anodic oxidation (MAO) with the thickness of 5−18 μm.[73] Overall, the anodized oxide layers on Mg prepared in this study showed a significantly higher interfacial adhesion strength when compared with other reports in the literature.[71−73] However, under an external shear force, the oxide layers on Mg prepared by EPD would be damaged more easily than the samples prepared by anodization because the interfacial adhesion strength of the EPD samples was at least 100 times less than that of the anodized samples.

3.2. Antimicrobial Properties of Nanostructured MgO on Mg Prepared by Anodization and EPD. The bacterial culture was carried out using a method modified from the JIS Z 2801 standard to simulate the situation of an infection that could occur in the primary surgery.[74] In the bacterial culture, we increased the volume of bacterial suspension to 50 μL instead of 20 or 36 μL described in the standard and literature,[74,75] because 50 μL was the maximum volume that the sample of 10 mm × 10 mm can hold on the top surface. Moreover, we added 1 mL of Tris buffer into each well of culture plates to retain moisture in the well during a 24-h incubation. The bacterial density adhered onto the samples and their corresponding filter papers was analyzed by counting the CFUs after a 24-h bacterial culture. The method of plating and counting CFUs is well accepted in microbiology for determining the bacterial viability.

Mg has been previously reported to reduce the growth of *S. aureus* when compared with the bacterial control and 316 stainless steel intramedullary pins (316LLS) in vitro.[76] In this study, no viable *S. aureus* was found on the surface of Mg. However, *S. aureus* on the filter paper on Mg still remained viable at a level of 10^3 CFU/mL, which was 0.02% of the bacterial seeding density. In contrast, the anodized Mg with a nanostructured MgO layer on the surface or the Mg coated with MgO nanoparticles by EPD killed all *S. aureus* on the sample surfaces and on the filter papers on the samples at the end of the 24-h culture in vitro, indicating a greater potency against bacterial adhesion than that on the nontreated metallic Mg surface. Despite the difference in surface morphology and surface roughness of the nanostructured oxide layers prepared by anodization and EPD, they showed a similar inhibitory effect on bacterial growth, probably because they were all hydrophilic and shared similar chemical compositions. Moreover, although the thicknesses of the nanostructured MgO layers on Mg prepared by anodization and EPD were different, they all showed similar bactericidal effects against *S. aureus*.

The kinetic studies on the antibacterial effects of the MgO microparticles and nanoparticles against *E. coli* and *S. epidermidis* have been reported previously.[77,78] For example, the death rate constant of the *E. coli* increased linearly in the 0−80 min of incubation with 1.25−20 mg/mL of MgO

microparticles at a temperature of 37 °C.[77] When *S. epidermidis* was exposed to 0.2 mg/mL MgO nanoparticles, the bacterial growth was inhibited when compared with the bacteria-only control based on their optical density (OD) readings, and the growth kinetics of *S. epidermidis* showed that the bacterial growth was delayed for a few hours initially and afterward partially inhibited when compared with the bacteria-only control in the 0−12 h of incubation.[78] However, the antibacterial kinetics of MgO nanoparticles or coatings against *S. aureus* has not been reported yet. For future studies, we recommend further kinetics analysis of the antibacterial effect of the nMgO-coated Mg in the 0−24 h of incubation time or longer if there were viable bacteria remaining.

3.3. Factors Affecting the Viability and Morphology of *S. aureus*. The factors influencing bacterial adhesion on implant surfaces include surface chemistry, surface charge, surface roughness, surface area, and hydrophilicity.[79] In this study, we mainly investigated the correlation between the surface properties of the biomaterials, such as surface chemistry, surface roughness/area, hydrophilicity, and their antimicrobial properties. MgO nanoparticles have shown antibacterial effects against both Gram-positive bacteria, i.e., *S. aureus*, *S. epidermidis*, and methicillin-resistant *S. aureus* (MRSA), and Gram-negative bacteria, i.e., *E. coli* and *P. aeruginosa*.[37,38] However, based on the previous study on *S. epidermidis*, a Gram-positive bacterium, the increases of broth pH up to 10 or Mg^{2+} concentrations up to 50 mM were not the main factors contributing to the antimicrobial properties of MgO nanoparticles.[38]

One proposed mechanism could be the contact between MgO and the bacteria that caused damage to the cell wall/membrane, leading to leakage of the internal minerals, proteins, and genetic materials.[37,38,80] For the Gram-positive bacteria, the positively charged MgO nanoparticles may interact with the negatively charged phosphate groups or trapped in the peptidoglycan layer of the bacteria, which may inhibit their growth.[38]

The oxidative stress and the produced intracellular reactive oxygen species (ROS) were also considered to be critical for the antibacterial activities of nanomaterials. Recently, Das et al. proved that the antibacterial effects of nanostructured MgO were ROS-dependent based on the peroxide (H_2O_2) detection.[81] Some bacteria such as *S. aureus* that undergo aerobic respiration also generate superoxide dismutase (SOD) to neutralize the ROS. If more ROS were produced and not timely neutralized by the SOD, the excess ROS could cause damage to the bacteria.[82−84] The ROS generation is dependent on the physicochemical properties of the nanomaterials, i.e., particle size, shape, surface area, chemical composition, degree of agglomerations, and the testing systems, i.e., bacterial types.[85,86] Among the physicochemical properties, the particle size, surface area, and chemical composition are the key factors for the production of ROS.[85] The decrease of particle size will lead to an increase of surface area because particle size and surface area are related. As the surface area increases, the number of active sites at which ROS generation can take place would increase.[85] In this study, the surface area of the nanostructured MgO layer produced using anodization is larger than that produced using the EPD method, as shown in Figure 6. Therefore, we speculated that the nanostructured MgO layer produced using anodization could generate a higher amount of ROS than that of the EPD method. Moreover, when the MgO nanoparticles inhibit the growth of the bacteria, they

may disrupt the quorum sensing among the bacteria because of the reduction in the number of bacteria in the culture suspension.[38] Previous studies in the literature[38,87−89] revealed that quorum sensing could affect bacterial properties such as virulence factors and the ability of bacteria to communicate to each other, inhibiting their activities and functions. Therefore, in our in vitro culture model of this study, the close contact of the bacteria with the nanostructured MgO might strengthen the interactions between the nanostructured MgO and the bacterial wall/membrane or increase the local ROS generated by the nanostructured MgO, thus killing the nearby bacteria within 24 h.

The surface roughness of biomaterials is another relevant factor that affects bacterial adhesion. Rougher surfaces at the micrometer scale normally promote bacterial adhesion due to the increased surface area that provides more sites for bacterial colonization.[79] In our previous study, the surface roughness of Mg control was 0.113 ± 0.006 μm,[41] which was significantly lower than the oxide layers produced by anodization and EPD. In this study, the rougher oxide surfaces produced via anodization and EPD showed better inhibitory effects on the growth of *S. aureus* when compared with the smoother nontreated surface of Mg control. This could be due to the synergic effect of surface chemistry, surface roughness and area, nanostructure, and hydrophilicity. The higher surface roughness and larger surface area of the oxide layers formed via anodization and EPD could lead to the increased presence of MgO nanostructures on the surface for disrupting bacterial activities.

Apart from surface chemistry and surface roughness of the implants, surface hydrophilicity also plays a significant role in biomaterial−bacterium interactions.[59] The thermodynamic theory suggested that the adhesion of *S. aureus* and *S. epidermidis* favored hydrophobicity of the biomaterial surface, which is considered to be the main driving force for general bacterial adhesion. Mackintosh et al. found that the adhesion of *S. epidermidis* after culturing with poly(ethylene terephthalate) (PET) in phosphate-buffered saline for 24 h was lower on the PET samples with hydrophilic modification when compared with that of the unmodified control and the other modified surfaces.[90] However, when the samples were incubated in serum in vitro, the hydrophilic, hydrophobic, and control surfaces all showed low bacterial adhesion.[90] One of the main reasons for the difference among these studies is that the protein absorption on biomaterials could alter their surface properties. Bare biomaterials would be coated with proteins from blood and interstitial fluids within nanoseconds when implanted.[33] Surface hydrophilicity could influence the bonding strength, conformation and orientation of proteins adhered to the surfaces, and composition of the macromolecular layer formed on the surfaces via selective adhesion from the biological fluid.[91,92] Therefore, the surface properties of biomaterials that affect protein adhesion and conformation could thus influence bacterial adhesion. In this study, the hydrophilic surface of the samples prepared by anodization and EPD, coupled with their surface chemistry, roughness, and nanostructures, could all contribute to the observed antibacterial effect in vitro.

We believe that MgO nanostructures created on Mg-based metals should have a bactericidal or inhibitory effect against many types of pathogenic microbes, such as Gram-positive bacteria (*S. aureus*, *S. epidermidis*, and MRSA), Gram-negative bacteria (*E. coli* and *P. aeruginosa*), and infectious yeasts [drug-

sensitive *Candida albicans*, fluconazole-resistant *C. albicans* (*C. albicans* FR), drug-sensitive *Candida glabrata*, and echinocandin-resistant *C. glabrata* (*C. glabrata* ER)], on the basis that MgO nanoparticles had a broad antimicrobial spectrum against all of these microbes.[37,38] In the future studies, it is still necessary to test all of these microbes with the nanostructured MgO on Mg substrates to determine the full-spectrum antimicrobial properties, because microbial interactions with the nano-MgO surface on Mg substrates may differ from MgO nanoparticles even though they both share the same chemistry of MgO.

3.4. Mg with Nanostructured MgO Surface Layer for Biomedical Applications.

The cytocompatibility and degradation performance of nanostructured MgO on Mg substrates prepared by anodization or EPD have been separately reported in our previous studies.[41,42] The specimens from both anodization and EPD have shown lower H_2 gas release than the polished bare Mg, and there are no adverse effects on BMSCs under indirect contact conditions of direct culture in vitro.[41,42] The significance of this study was to elucidate the relationships between the two different processing methods and the resulted differences in surface properties for the first time. Specifically, we investigated and compared the surface properties including microstructures, surface roughness and area, surface wettability, and interfacial adhesion strength of the surface oxide layers on the Mg substrates prepared by anodization versus EPD. Moreover, in this study, we discussed the correlation between the surface properties and the bactericidal effects of the prepared samples and first reported the synergic effects of the surface chemistry of nanostructured MgO, surface roughness and surface area, and hydrophilicity of the prepared samples on reducing bacterial adhesion and growth. This study confirmed the critical hypothesis regarding the bactericidal properties of the nanostructured oxide layers on pure Mg. The killing effect of the surface-treated Mg by anodization and EPD against *S. aureus* is very promising for preventing severe infections and associated complications in medical implants, especially in the cases of trauma surgeries for open wounds. Moreover, the nanostructured MgO on Mg prepared using the anodization method showed much stronger interfacial adhesion strength than that of the EPD method, thus being more favorable for medical implant applications.

Remarkable progress has been made in the developments of Mg-based biomaterials and clinical translation in recent years, especially Mg−RE alloys. The clinical application of the MgYREZr screw has first been reported in Germany for treatments of mild hallux valgus, demonstrating better biocompatibility and osteoconductive properties when compared with that of Ti screws.[10] More recently, the MgYREZr screw was used in the fixation of distal fibular fractures and intra-articular fractures in clinical case studies, and the results have shown complete fracture healing and free range of motion in the patients.[11,12] To further optimize the collective properties of Mg-based implants including degradation properties, biocompatibility, bioactivity, and antimicrobial properties, our methodology for developing nanostructured oxide layers could be applied to the Mg−RE alloys or any other kinds of Mg alloys.

The collective properties of the surface-treated Mg by anodization and EPD in cytocompatibility, degradation performance, and antimicrobial activities are promising for biomedical implant applications. The mechanisms for the bactericidal properties of the developed MgO nanostructures

on Mg were mainly discussed based on the literature. Further experiments will be needed to determine the specific contributions of the proposed mechanisms, such as bacterial membrane damage, ROS generation, and quorum sensing disruption caused by MgO surface chemistry, surface roughness and surface area, and wettability. Moreover, the performance of the nanostructured MgO on Mg requires further studies in vivo because the different conditions in vivo such as high shear stress in different anatomical sites could influence bacterial behaviors, e.g., the rates of horizontal gene transfer and mutations.[33] Therefore, it is necessary to perform in vivo studies in a functional animal model with infection for the nanostructured MgO on Mg-based metals toward clinical translation.

4. CONCLUSIONS

This article reported the surface morphology, elemental composition, crystalline phases, surface roughness, surface area, surface wettability, interfacial adhesion strength between the surface oxide layers and the underlying Mg substrates, and antimicrobial properties of nanostructured MgO on Mg prepared by respective anodization and EPD processes, that is, 1.9 A, 1.9 AA, EPD, and A-EPD samples. The anodized Mg samples of 1.9 A and 1.9 AA showed superior interfacial adhesion strength between the MgO surface layers and the underlying Mg substrates than the samples prepared by EPD and A-EPD processes. The strong interfacial adhesion of the nanostructured MgO surface layer to the underlying Mg substrate could lead to better performance in clinical applications, including improved biocompatibility, corrosion resistance, and antibacterial activity, for the 1.9 A and 1.9 AA samples, during in vivo implantation. The in vitro bacterial study of the surface-treated Mg against *S. aureus* showed impressive bactericidal effects, indicating a great potential in reducing device-associated infections in many clinical areas. The mechanisms of bactericidal effects could be related to the surface chemistry coupled with the surface roughness, surface area, and hydrophilicity, which enhanced the functions of the ROS generated by the MgO nanostructures, and the interactions between MgO nanostructures and bacterial wall/membrane. Further studies are needed to elucidate the exact mechanisms. In the future, it is necessary to perform in vivo studies in an infected animal model for the validation of nanostructured MgO on Mg-based metals for reducing infection while promoting healing.

5. MATERIALS AND METHODS

5.1. Anodization and Electrophoretic Deposition (EPD) Process.

The methods for creating MgO nanostructures on Mg substrates using anodization[41] and EPD[42] have been previously established and adapted for this study as described below with permission from the publishers.[41,42]

5.1.1. Preparation of Mg Substrates as Electrodes for Anodization and EPD. Commercially pure magnesium sheets (99.9 wt% purity, as-rolled, 1.0 mm thick, Cat# 40604; Alfa Aesar, Ward Hill, MA) were used for this study. The magnesium sheets were cut into 10 mm × 10 mm squares, connected to the copper wires using copper tapes and embedded in epoxy resin (Cat# ULTRA-3000R-32; Pace Technologies, Tucson, AZ) to ensure that only one surface with a dimension of 10 mm × 10 mm was exposed, as shown in the previous study.[41] The exposed surface of the embedded

Mg was ground with 240, 600, 800, and 1200 grit SiC adhesive papers (Ted Pella Inc., Redding, CA) and polished using the polycrystalline diamond paste of up to 0.25 μm (Physical Test Solutions, Culver City, CA). The well-polished surface of embedded Mg was ultrasonically cleaned in acetone and ethanol for 30 min each, before the anodization and EPD processes.

5.1.2. Experimental Setup for Anodization and EPD. A three-electrode system was used for anodization. The embedded Mg was used as the working electrode (anode), a platinum plate was used as the cathode, and Ag/AgCl was used as the reference electrode. The electrodes were connected to a potentiostat (model 273A; Princeton Applied Research, Oak Ridge, TN) that was controlled by a Powersuite 2.50.0 software (Princeton Applied Research). The distance between the cathode and anode was 1 cm. The working electrode was anodized in a 10 M KOH electrolyte at 1.9 V at room temperature for 2 h. The resulted sample was referred to as 1.9 A; the suffix "A" represents "as-anodized". As for the electrophoretic deposition process, a two-electrode system was used. The embedded Mg was used as the cathode and a platinum (Pt) plate was used as an anode. The distance between the cathode and anode was 1 cm. The high-power probe sonicator (model S-4000, Misonix) was used to sonicate 3 mg/mL MgO nanoparticles in anhydrate ethanol in duty cycles of 5 s on and 5 s off for 5 min to avoid agglomeration and ensure a stable homogeneous suspension for the EPD process. The MgO nanoparticles were deposited onto the working electrode of Mg at a voltage of 23 V/cm for 60 s at room temperature. The resulted sample was referred to as "EPD".

5.1.3. Sample Annealing After Anodization and EPD. The annealing process was the same as described in our previous study.[41] The samples prepared by anodization or EPD were removed from the epoxy resin using a notcher (no. 100, Whitney Metal Tool Co.) and subsequently annealed at 450 °C for 6 h in a tube furnace in an argon atmosphere to convert the Mg(OH)$_2$ to MgO through a dehydration reaction. During the annealing process, the temperature increased from room temperature to 450 °C with a heating rate of 100 °C/h to avoid the sudden collapse of Mg(OH)$_2$ crystal structure and was held at 450 °C for 6 h. Afterward, the tube furnace was turned off to cool down naturally. After annealing, the resulted sample prepared by anodization and EPD was referred to as "1.9 AA" and "A-EPD"; the addition of suffix "A" or prefix "A" represents "annealed". The anodized samples before annealing were referred to as "1.9 A", and the samples prepared by EPD before annealing were referred to as "EPD".

5.2. Surface and Cross-Sectional Characterization. After annealing, the samples were sputter-coated (model 108, Cressington Scientific Instruments Ltd., Watford, U.K.) with platinum/palladium at 20 mA with a 40 s sputter time. A scanning electron microscope (SEM; Nova NanoSEM 450, FEI Co., Hillsboro, OR) was used to characterize the surface morphology and cross sections of the oxide layers on Mg substrates. Energy-dispersive X-ray spectroscopy (EDS, X-Max50) and AztecEnergy software (Oxford Instruments, Abingdon, Oxfordshire, U.K.) were used to analyze the surface elemental composition and distribution. SEM images for the surfaces were taken in the Everhart−Thornley detector (ETD) mode with an acceleration voltage of 20 kV with a working distance of 5 mm and original magnifications of 150×, 10 000×, and 40 000×. EDS analysis was performed with an

accelerating voltage of 10 kV at an original magnification of 150×. Different acceleration voltages were used for SEM and EDS because more signals from the surface coatings can be detected at a lower acceleration voltage (10 kV), while more signals from the underlying Mg substrates can be detected at a higher acceleration voltage (20 kV). To analyze the cross sections and determine the thickness of the surface-treated Mg after annealing, the samples were cut into half and mounted onto a 90° SEM sample holder, sputter-coated under the same conditions as mentioned above, and analyzed using SEM and EDS at an acceleration voltage of 20 kV, a working distance of 5 mm, and an original magnification of 2000×. The thickness of the MgO layers on Mg substrates was quantified using the ImageJ software.

X-ray diffraction (XRD; Empyrean, PANalytical, Westborough, MA) was used to analyze the phases and crystal structures of the samples. All XRD spectra were acquired using Cu Kα radiation (45 kV, 40 mA) at a step size of 0.01° and a dwelling time of 30 s using a PIXcel 1D detector (PANalytical). Phase identification was performed using the HighScore software (PANalytical).

5.3. Microscratch Testing of the nMgO on Mg Prepared by Anodization and EPD. The interfacial adhesion strength of the prepared samples was evaluated using the Microscratchtester (Nanovea, Irvine, CA) equipped with a sphero-conical stainless steel stylus with an outer diameter (OD) of 1.5 mm. The load on the stainless steel stylus linearly increased from 0 to 150 N at a normal loading speed of 300 N/min when the stylus was drawn across the surface of the coating at a distance of 2 mm. The drawing speed of the stylus was 4 mm/min. After scratching, the coating surface was analyzed under an optical microscope to examine the initial position where the oxide layers delaminated. The normal load and frictional force versus scratch distance were analyzed to determine the critical load (L_f), which is the force at which the initial delamination occurred.

5.4. Surface Roughness, Surface Area, and Contact Angle Measurements. The surface topography of 1.9 A, 1.9 AA, EPD, and A-EPD samples was characterized using a 3D laser scanning microscope (VK-X150, Keyence), and the surface roughness (S_q) and surface area (SA) were measured using the MultifileAnalyzer software (VK-H1XME, Keyence) following our previously established method.[93]

The surface wettability of the samples was measured using a contact angle goniometer (EasyDrop; Krüss) in the ambient environment. For the contact angle measurement, 3 μL of tryptic soy broth (TSB; Fluka Analytical, Sigma-Aldrich) was dropped on the sample surface and the images were taken. The video recordings were saved to the connected computer where the contact angles were analyzed using a drop shape analyzer (DSA 100, Krüss). The measurements were repeated at three different locations on each sample.

5.5. Antimicrobial Study with *S. aureus* In Vitro. The method used for this in vitro antimicrobial study was adapted from the Japanese Industrial Standard JIS Z 2801:2000,[57] since it has been validated for testing antimicrobial properties of various samples in the literature, including surface-treated titanium (Ti) alloys and surface-treated polymer substrates.[74,75,94,95] As illustrated in Figure 1, this in vitro method was used to determine the antimicrobial properties of the prepared samples against *S. aureus*. The prepared samples were disinfected under ultraviolet (UV) radiation for 2 h prior to the bacterial culture. Polished Mg without surface treatment (i.e.,

without anodization and EPD) and polished titanium (99.99 wt% purity, 1.0 mm thick; Alfa Aesar) were included in the bacterial culture as the controls, and glass was included as a reference. The Mg and titanium controls were ground with 240, 600, 800, and 1200 grit SiC adhesive papers and polished using the polycrystalline diamond paste of up to 0.25 μm. The Mg and titanium controls and glass reference were ultrasonically cleaned in acetone and ethanol for 30 min each, followed by disinfection under UV for 2 h. Specific details on the bacterial culture methods were described previously.[38] Briefly, a portion of the frozen stock of *S. aureus* stored at −80 °C. was transported to 10 mL of TSB in a 50 mL centrifuge tube using a sterilized loop. The bacteria were cultured in TSB using a shaker incubator (Incu-Shaker Mini, Benchmark Scientific) at 37 °C and 250 rpm for 16 h. An aliquot of 100 μL of *S. aureus* was added to fresh TSB and cultured for another 4−6 h. After that, the concentration of bacteria in the working stock was determined using a hemocytometer (Hausser Bright-Line 3200, Hausser Scientific) and diluted to a concentration of 7.8 × 10^6 cells/mL in TSB because this concentration is clinically relevant for orthopedic implant infections.[96] To confirm the actual seeding density of *S. aureus*, the working stock was diluted in 10 000 times using Tris(hydroxymethyl)-aminomethane buffer (Tris buffer; Acros, Sigma-Aldrich) and 100 μL of the suspension was plated on the tryptic soy agar (TSA; Fluka Analytical, Sigma-Aldrich). The agar plates were incubated at 37 °C for 24 h, and the colony forming units (CFUs) on the agar plates were counted to calculate the actual seeding density. The actual seeding density of *S. aureus* in this study was 6 × 10^6 CFU/mL, close to the prescribed seeding density. Sterilized nitrocellulose filter papers had a diameter of 1 cm and were placed on an agar plate, and the diluted *S. aureus* of 50 μL, containing 6 × 10^6 CFU/mL, was pipetted onto the filter papers. TSB was absorbed by the agar and *S. aureus* retained on the filter paper (Figure 1). TSB of 50 μL was pipetted onto the center of each sample surface, and the inoculated filter paper was carefully placed on top of the sample so that the *S. aureus* became in contact with the sample surface. The filter paper with *S. aureus* fit as an inscribed circle on the 1 × 1 cm^2 square-shaped samples. Each sample with a filter paper on its surface was placed on a three-dimensional (3D) printed holder in a well of non-tissue-culture treated plates and incubated at 37 °C for 24 h. Afterward, 1 mL of Tris buffer was added into each well to retain humidity for the 24-h bacterial incubation. The schematic illustration of the 3D printed sample holder and its dimensions (diameter: 15 mm, height: 10 mm) is shown in Figure 1. The bacteria-only without samples and TSB-only without bacteria and samples were incubated as the positive control and blank reference, respectively. After 24 h, the filter paper on each sample and the corresponding sample were placed individually into 5 mL of Tris buffer, vortexed for 5 s, and sonicated for 5 min twice to dislodge the adhered bacteria. After that, the Tris buffer containing the bacteria dislodged from the samples or the corresponding filter papers were serially diluted and 100 μL of the diluted and nondiluted suspensions was spread onto the tryptic soy agar plates. The agar plates were incubated in the shaker incubator (without shaking) at 37 °C for 24 h, and the colony forming unit (CFU) on each agar plate was counted. The bacterial concentration was determined by measuring the CFUs on agar plates. The bacterial study was run in triplicate for each type of samples.

5.6. Bacterial Adhesion and Morphology After a 24-h Culture with the Samples. After 24 h of bacterial culture, one sample from each group was washed three times with Tris buffer and transferred to a new well plate. Free bacteria that did not attach onto the sample were washed away. After the third wash, the bacteria on the sample were fixed with 10% glutaraldehyde for 1 h. The 10% glutaraldehyde was diluted previously from a 25% glutaraldehyde solution (Sigma Life Sciences, Sigma-Aldrich) in Tris buffer. After 1 h, each sample was rinsed three times with Tris buffer to remove any glutaraldehyde residue, dehydrated using 30, 75, and 100% ethanol for 30 min each, and then air-dried at room temperature for 24 h. The dried samples were sputter-coated with Pt/Pd using a sputter coater (108 Auto Sputter Coater, Cressington Scientific) at 20 mA for 45 s, prior to the SEM imaging. Representative images were taken using the same SEM described above, with a secondary electron detector at an accelerating voltage of 10 kV, a working distance of 5 mm, and original magnifications of 150× and 5000×. The surface elemental composition of the samples after bacterial culture was analyzed using EDS at an accelerating voltage of 10 kV and an original magnification of 150×. The phases and crystal structures of the samples after bacterial culture were analyzed using the same XRD as described in Section 5.2, with the PIXcel 1D detector at a step size of 0.01° and a dwelling time of 30 s. Phase identification was performed using the HighScore software.

5.7. Statistical Analyses. All numerical data in this study were obtained from experiments run in triplicate. The numerical data were examined using one-way analysis of variance (ANOVA) followed by a Tukey test, when the data sets fulfilled the parametric criteria (i.e., data normality was over 0.5). Statistical significance was considered at $p < 0.05$ for the Tukey test. For nonparametric data (i.e., data normality was less than 0.5), the data sets were examined using the Kruskal−Wallis analyses followed by a Dunn test and adjusted by Hochberg's method. Statistical significance was considered at $p < 0.025$ for the Dunn test.

■ AUTHOR INFORMATION

Corresponding Author

Huinan Hannah Liu − *Material Science & Engineering Program, Microbiology Program, and Department of Bioengineering, University of California, Riverside, Riverside, California 92521, United States;* ● orcid.org/0000-0001-9366-6204; Phone: 951 827 2944; Email: huinan.liu@ucr.edu; Fax: 951 827 6416

Authors

Jiajia Lin − *Material Science & Engineering Program, University of California, Riverside, Riverside, California 92521, United States*

Nhu-Y Thi Nguyen − *Microbiology Program, University of California, Riverside, Riverside, California 92521, United States*

Chaoxing Zhang − *Material Science & Engineering Program, University of California, Riverside, Riverside, California 92521, United States;* ● orcid.org/0000-0003-4115-7111

Alexandra Ha − *Department of Bioengineering, University of California, Riverside, Riverside, California 92521, United States*

Complete contact information is available at:
https://pubs.acs.org/10.1021/acsomega.0c03151

Notes

The authors declare no competing financial interest.

■ REFERENCES

(1) Cipriano, A. F.; Lin, J.; Lin, A.; Sallee, A.; Le, B.; Cortez Alcaraz, M. C.; Guan, R.-G.; Botimer, G.; Inceoğlu, S.; Liu, H. Degradation of Bioresorbable Mg−4Zn−1Sr Intramedullary Pins and Associated Biological Responses in Vitro and in Vivo. *ACS Appl. Mater. Interfaces* **2017**, *9*, 44332−44355.

(2) Trumbo, P.; Schlicker, S.; Yates, A. A.; Poos, M. Dietary reference intakes for energy, carbohdrate, fiber, fat, fatty acids, cholesterol, protein and amino acids. *J. Acad. Nutr. Diet.* **2002**, *102*, 1621.

(3) Song, M.-S.; Zeng, R.-C.; Ding, Y.-F.; Li, R. W.; Easton, M.; Cole, I.; Birbilis, N.; Chen, X.-B. Recent advances in biodegradation controls over Mg alloys for bone fracture management: a review. *J. Mater. Sci. Technol.* **2019**, *35*, 535−544.

(4) Geetha, M.; Singh, A. K.; Asokamani, R.; Gogia, A. K. Ti based biomaterials, the ultimate choice for orthopaedic implants—a review. *Prog. Mater. Sci.* **2009**, *54*, 397−425.

(5) Chen, Q.; Thouas, G. A. Metallic implant biomaterials. *Mater. Sci. Eng., R* **2015**, *87*, 1−57.

(6) Hornberger, H.; Virtanen, S.; Boccaccini, A. Biomedical coatings on magnesium alloys—a review. *Acta Biomater.* **2012**, *8*, 2442−2455.

(7) Riaz, U.; Shabib, I.; Haider, W. The current trends of Mg alloys in biomedical applications—A review. *J. Biomed. Mater. Res., Part B* **2019**, *107*, 1970−1996.

(8) Zhao, D.; Witte, F.; Lu, F.; Wang, J.; Li, J.; Qin, L. Current status on clinical applications of magnesium-based orthopaedic implants: A review from clinical translational perspective. *Biomaterials* **2017**, *112*, 287−302.

(9) Chen, Y.; Xu, Z.; Smith, C.; Sankar, J. Recent advances on the development of magnesium alloys for biodegradable implants. *Acta Biomater.* **2014**, *10*, 4561−4573.

(10) Windhagen, H.; Radtke, K.; Weizbauer, A.; Diekmann, J.; Noll, Y.; Kreimeyer, U.; Schavan, R.; Stukenborg-Colsman, C.; Waizy, H. Biodegradable magnesium-based screw clinically equivalent to titanium screw in hallux valgus surgery: short term results of the first prospective, randomized, controlled clinical pilot study. *Biomed. Eng. Online* **2013**, *12*, No. 62.

(11) Biber, R.; Pauser, J.; Brem, M.; Bail, H. J. Bioabsorbable metal screws in traumatology: a promising innovation. *Trauma Case Rep.* **2017**, *8*, 11−15.

(12) Biber, R.; Pauser, J.; Geßlein, M.; Bail, H. J. Magnesium-based absorbable metal screws for intra-articular fracture fixation. *Case Rep. Orthop.* **2016**, *2016*, No. 9673174.

(13) Han, P.; Cheng, P.; Zhang, S.; Zhao, C.; Ni, J.; Zhang, Y.; Zhong, W.; Hou, P.; Zhang, X.; Zheng, Y.; Chai, Y. In vitro and in

vivo studies on the degradation of high-purity Mg (99.99 wt.%) screw with femoral intracondylar fractured rabbit model. *Biomaterials* **2015**, *64*, 57−69.

(14) Huang, S.; Wang, B.; Zhang, X.; Lu, F.; Wang, Z.; Tian, S.; Li, D.; Yang, J.; Cao, F.; Cheng, L.; et al. High-purity weight-bearing magnesium screw: Translational application in the healing of femoral neck fracture. *Biomaterials* **2020**, *238*, No. 119829.

(15) Zhao, D.; Huang, S.; Lu, F.; Wang, B.; Yang, L.; Qin, L.; Yang, K.; Li, Y.; Li, W.; Wang, W.; et al. Vascularized bone grafting fixed by biodegradable magnesium screw for treating osteonecrosis of the femoral head. *Biomaterials* **2016**, *81*, 84−92.

(16) Han, H.-S.; Loffredo, S.; Jun, I.; Edwards, J.; Kim, Y.-C.; Seok, H.-K.; Witte, F.; Mantovani, D.; Glyn-Jones, S. Current status and outlook on the clinical translation of biodegradable metals. *Mater. Today* **2019**, *23*, 57−71.

(17) Kumar, K.; Gill, R.; Batra, U. Challenges and opportunities for biodegradable magnesium alloy implants. *Mater. Technol.* **2018**, *33*, 153−172.

(18) Poinern, G. E. J.; Brundavanam, S.; Fawcett, D. Biomedical magnesium alloys: a review of material properties, surface modifications and potential as a biodegradable orthopaedic implant. *Am. J. Biomed. Eng.* **2012**, *2*, 218−240.

(19) Noviana, D.; Paramitha, D.; Ulum, M. F.; Hermawan, H. The effect of hydrogen gas evolution of magnesium implant on the postimplantation mortality of rats. *J. Orthop. Transl.* **2016**, *5*, 9−15.

(20) Lee, J.-W.; Han, H.-S.; Han, K.-J.; Park, J.; Jeon, H.; Ok, M.-R.; Seok, H.-K.; Ahn, J.-P.; Lee, K. E.; Lee, D.-H.; et al. Long-term clinical study and multiscale analysis of in vivo biodegradation mechanism of Mg alloy. *Proc. Natl. Acad. Sci. U.S.A.* **2016**, *113*, 716−721.

(21) Abisegapriyan, K. S.; Rajeshwari, A.; Kundu, S.; Subramanian, B. Magnesium glassy alloy laminated nanofibrous polymer as biodegradable scaffolds. *J. Non-Cryst. Solids* **2018**, *502*, 210−217.

(22) Jia, Z.; Xiu, P.; Xiong, P.; Zhou, W.; Cheng, Y.; Wei, S.; Zheng, Y.; Xi, T.; Cai, H.; Liu, Z.; et al. Additively manufactured macroporous titanium with silver-releasing micro-/nanoporous surface for multipurpose infection control and bone repair—a proof of concept. *ACS Appl. Mater. Interfaces* **2016**, *8*, 28495−28510.

(23) Darouiche, R. O. Treatment of infections associated with surgical implants. *N. Engl. J. Med.* **2004**, *350*, 1422−1429.

(24) Campoccia, D.; Montanaro, L.; Arciola, C. R. The significance of infection related to orthopedic devices and issues of antibiotic resistance. *Biomaterials* **2006**, *27*, 2331−2339.

(25) Oliveira, W.; Silva, P.; Silva, R.; Silva, G.; Machado, G.; Coelho, L.; Correia, M. *Staphylococcus aureus* and *Staphylococcus epidermidis* infections on implants. *J. Hosp. Infect.* **2018**, *98*, 111−117.

(26) Raphel, J.; Holodniy, M.; Goodman, S. B.; Heilshorn, S. C. Multifunctional coatings to simultaneously promote osseointegration and prevent infection of orthopaedic implants. *Biomaterials* **2016**, *84*, 301−314.

(27) Costerton, J. W.; Stewart, P. S.; Greenberg, E. P. Bacterial biofilms: a common cause of persistent infections. *Science* **1999**, *284*, 1318−1322.

(28) Hall-Stoodley, L.; Costerton, J. W.; Stoodley, P. Bacterial biofilms: from the natural environment to infectious diseases. *Nat. Rev. Microbiol.* **2004**, *2*, 95.

(29) Sabaté Brescó, M.; Harris, L. G.; Thompson, K.; Stanic, B.; Morgenstern, M.; O'Mahony, L.; Richards, R. G.; Moriarty, T. F. Pathogenic mechanisms and host interactions in *Staphylococcus epidermidis* device-related infection. *Front. Microbiol.* **2017**, *8*, No. 1401.

(30) Valstar, E. R.; Nelissen, R. G.; Reiber, J. H.; Rozing, P. M. The use of Roentgen stereophotogrammetry to study micromotion of orthopaedic implants. *ISPRS J. Photogramm. Remote Sens.* **2002**, *56*, 376−389.

(31) Gristina, A. G. Biomaterial-centered infection: microbial adhesion versus tissue integration. *Science* **1987**, *237*, 1588−1595.

(32) Boles, B. R.; Horswill, A. R. Agr-mediated dispersal of *Staphylococcus aureus* biofilms. *PLoS Pathog.* **2008**, *4*, No. e1000052.

(33) Arciola, C. R.; Campoccia, D.; Montanaro, L. Implant infections: adhesion, biofilm formation and immune evasion. *Nat. Rev. Microbiol.* **2018**, *16*, 397.

(34) Otto, M. Staphylococcal biofilms. *Curr. Top. Microbiol. Immunol.* **2008**, *322*, 207−228.

(35) Sawai, J.; Kojima, H.; Igarashi, H.; Hashimoto, A.; Shoji, S.; Sawaki, T.; Hakoda, A.; Kawada, E.; Kokugan, T.; Shimizu, M. Antibacterial characteristics of magnesium oxide powder. *World J. Microbiol. Biotechnol.* **2000**, *16*, 187−194.

(36) Sawai, J. Quantitative evaluation of antibacterial activities of metallic oxide powders (ZnO, MgO and CaO) by conductimetric assay. *J. Microbiol. Methods* **2003**, *54*, 177−182.

(37) Wetteland, C. L.; Nguyen, N.-Y. T.; Liu, H. Concentration-dependent behaviors of bone marrow derived mesenchymal stem cells and infectious bacteria toward magnesium oxide nanoparticles. *Acta Biomater.* **2016**, *35*, 341−356.

(38) Nguyen, N.-Y. T.; Grelling, N.; Wetteland, C. L.; Rosario, R.; Liu, H. Antimicrobial Activities and Mechanisms of Magnesium Oxide Nanoparticles (nMgO) against Pathogenic Bacteria, Yeasts, and Biofilms. *Sci. Rep.* **2018**, *8*, No. 16260.

(39) Hickey, D. J.; Muthusamy, D.; Webster, T. J. Electrophoretic deposition of MgO nanoparticles imparts antibacterial properties to poly-L-lactic acid for orthopedic applications. *J. Biomed. Mater. Res. A* **2017**, *105*, 3136−3147.

(40) Ricker, A.; Liu-Snyder, P.; Webster, T. J. The influence of nano MgO and BaSO4 particle size additives on properties of PMMA bone cement. *Int. J. Nanomed.* **2008**, *3*, 125.

(41) Cipriano, A. F.; Lin, J.; Miller, C.; Lin, A.; Alcaraz, M. C. C.; Soria, P., Jr.; Liu, H. Anodization of magnesium for biomedical applications−Processing, characterization, degradation and cytocompatibility. *Acta Biomater.* **2017**, *62*, 397−417.

(42) Cortez Alcaraz, M. C.; Cipriano, A. F.; Lin, J.; Soria, P., Jr.; Tian, Q.; Liu, H. Electrophoretic Deposition of Magnesium Oxide Nanoparticles on Magnesium: Processing Parameters, Microstructures, Degradation, and Cytocompatibility. *ACS Appl. Bio Mater* **2019**, *2*, 5634−5652.

(43) Lindström, R.; Johansson, L.-G.; Thompson, G. E.; Skeldon, P.; Svensson, J.-E. Corrosion of magnesium in humid air. *Corros. Sci.* **2004**, *46*, 1141−1158.

(44) Avedesian, M.; Baker, H., Eds. *ASM Specialty Handbook: Magnesium and Magnesium Alloys*; ASM International, 1999; pp 106−118.

(45) Nordlien, J. H.; Nisancioglu, K.; Ono, S.; Masuko, N. Morphology and structure of water-formed oxides on ternary MgAl alloys. *J. Electrochem. Soc.* **1997**, *144*, 461−466.

(46) Miley, H. Fundamentals of Oxidation and Tarnish. *The Corrosion Handbook*; John Wiley: New York, 1948; pp 11−20.

(47) Asami, K.; Ono, S. Quantitative X-Ray Photoelectron Spectroscopy Characterization of Magnesium Oxidized in Air. *J. Electrochem. Soc.* **2000**, *147*, 1408−1413.

(48) Seyeux, A.; Liu, M.; Schmutz, P.; Song, G.; Atrens, A.; Marcus, P. ToF-SIMS depth profile of the surface film on pure magnesium formed by immersion in pure water and the identification of magnesium hydride. *Corros. Sci.* **2009**, *51*, 1883−1886.

(49) Barchiche, C.-E.; Rocca, E.; Juers, C.; Hazan, J.; Steinmetz, J. Corrosion resistance of plasma-anodized AZ91D magnesium alloy by electrochemical methods. *Electrochim. Acta* **2007**, *53*, 417−425.

(50) Gray, J.; Luan, B. Protective coatings on magnesium and its alloys—a critical review. *J. Alloys Compd.* **2002**, *336*, 88−113.

(51) Zhu, Y.; Wu, G.; Zhang, Y.-H.; Zhao, Q. Growth and characterization of Mg (OH) 2 film on magnesium alloy AZ31. *Appl. Surf. Sci.* **2011**, *257*, 6129−6137.

(52) Tian, P.; Liu, X. Surface modification of biodegradable magnesium and its alloys for biomedical applications. *Regener. Biomater.* **2015**, *2*, 135−151.

(53) Li, B.; Gao, P.; Zhang, H.; Guo, Z.; Zheng, Y.; Han, Y. Osteoimmunomodulation, osseointegration, and in vivo mechanical integrity of pure Mg coated with HA nanorod/pore-sealed MgO bilayer. *Biomater. Sci.* **2018**, *6*, 3202−3218.

(54) Wang, J.; Tang, J.; Zhang, P.; Li, Y.; Wang, J.; Lai, Y.; Qin, L. Surface modification of magnesium alloys developed for bioabsorbable orthopedic implants: a general review. *J. Biomed. Mater. Res., Part B* **2012**, *100B*, 1691−1701.

(55) Moreno, R.; Ferrari, B. Nanoparticles Dispersion and the Effect of Related Parameters in the EPD Kinetics. *Electrophoretic Deposition of Nanomaterials*; Springer: New York, 2012; pp 73−128.

(56) Blawert, C.; Dietzel, W.; Ghali, E.; Song, G. Anodizing treatments for magnesium alloys and their effect on corrosion resistance in various environments. *Adv. Eng. Mater.* **2006**, *8*, 511−533.

(57) Japanese Standards Association. *JIS Z 2801:2000, Antimicrobial Products−Test for Antimicrobial Activity and Efficacy*; Japanese Standards Association, 2000.

(58) Zhang, C.; Lin, J.; Nguyen, N.-Y. T.; Guo, Y.; Xu, C.; Seo, C.; Villafana, E.; Jimenez, H.; Chai, Y.; Guan, R. Antimicrobial Bioresorbable Mg−Zn−Ca Alloy for Bone Repair in a Comparison Study with Mg−Zn−Sr Alloy and Pure Mg. *ACS Biomater. Sci. Eng.* **2019**, *517*.

(59) Gittens, R. A.; Scheideler, L.; Rupp, F.; Hyzy, S. L.; Geis-Gerstorfer, J.; Schwartz, Z.; Boyan, B. D. A review on the wettability of dental implant surfaces II: Biological and clinical aspects. *Acta Biomater.* **2014**, *10*, 2907−2918.

(60) Lei, T.; Ouyang, C.; Tang, W.; Li, L.-F.; Zhou, L.-S. Preparation of MgO coatings on magnesium alloys for corrosion protection. *Surf. Coat. Technol.* **2010**, *204*, 3798−3803.

(61) Lei, T.; Ouyang, C.; Tang, W.; Li, L.-F.; Zhou, L.-S. Enhanced corrosion protection of MgO coatings on magnesium alloy deposited by an anodic electrodeposition process. *Corros. Sci.* **2010**, *52*, 3504−3508.

(62) Wenzel, R. N. Resistance of solid surfaces to wetting by water. *Ind. Eng. Chem.* **1936**, *28*, 988−994.

(63) Mel'gunov, M. S.; Fenelonov, V. B.; Mel'gunova, E. A.; Bedilo, A. F.; Klabunde, K. J. Textural changes during topochemical decomposition of nanocrystalline Mg(OH)2 to MgO. *J. Phys. Chem. B* **2003**, *107*, 2427−2434.

(64) Johnson, I.; Lin, J.; Liu, H. Surface Modification and Coatings for Controlling the Degradation and Bioactivity of Magnesium Alloys for Medical Applications. *Orthopedic Biomaterials*; Springer: New York, 2017; pp 331−363.

(65) Gawlik, M. M.; Wiese, B.; Desharnais, V.; Ebel, T.; Willumeit-Römer, R. The Effect of Surface Treatments on the Degradation of Biomedical Mg Alloys—A Review Paper. *Materials* **2018**, *11*, 2561.

(66) Wang, S.; Lacefield, W. R.; Lemons, J. E. Interfacial shear strength and histology of plasma sprayed and sintered hydroxyapatite implants in vivo. *Biomaterials* **1996**, *17*, 1965−1970.

(67) Feng, J.; Chen, Y.; Liu, X.; Liu, T.; Zou, L.; Wang, Y.; Ren, Y.; Fan, Z.; Lv, Y.; Zhang, M. In-situ hydrothermal crystallization Mg (OH) 2 films on magnesium alloy AZ91 and their corrosion resistance properties. *Mater. Chem. Phys.* **2013**, *143*, 322−329.

(68) Yang, Y.-C.; Chang, E. Influence of residual stress on bonding strength and fracture of plasma-sprayed hydroxyapatite coatings on Ti−6Al−4V substrate. *Biomaterials* **2001**, *22*, 1827−1836.

(69) Gnedenkov, S.; Khrisanfova, O.; Zavidnaya, A.; Sinebryukhov, S.; Egorkin, V.; Nistratova, M.; Yerokhin, A.; Matthews, A. PEO coatings obtained on an Mg−Mn type alloy under unipolar and bipolar modes in silicate-containing electrolytes. *Surf. Coat. Technol.* **2010**, *204*, 2316−2322.

(70) Srinivasan, P. B.; Liang, J.; Blawert, C.; Störmer, M.; Dietzel, W. Characterization of calcium containing plasma electrolytic oxidation coatings on AM50 magnesium alloy. *Appl. Surf. Sci.* **2010**, *256*, 4017−4022.

(71) Durdu, S.; Usta, M. Characterization and mechanical properties of coatings on magnesium by micro arc oxidation. *Appl. Surf. Sci.* **2012**, *261*, 774−782.

(72) Aktuğ, S. L.; Durdu, S.; Kutbay, I.; Usta, M. Effect of Na2SiO3·5H2O concentration on microstructure and mechanical properties of plasma electrolytic oxide coatings on AZ31 Mg alloy produced by twin roll casting. *Ceram. Int.* **2016**, *42*, 1246−1253.

(73) Mandelli, A.; Bestetti, M.; Da Forno, A.; Lecis, N.; Trasatti, S.; Trueba, M. A composite coating for corrosion protection of AM60B magnesium alloy. *Surf. Coat. Technol.* **2011**, *205*, 4459−4465.

(74) Necula, B. S.; Fratila-Apachitei, L. E.; Zaat, S. A.; Apachitei, I.; Duszczyk, J. In vitro antibacterial activity of porous TiO_2−Ag composite layers against methicillin-resistant *Staphylococcus aureus*. *Acta Biomater.* **2009**, *5*, 3573−3580.

(75) Cleophas, R. T.; Sjollema, J.; Busscher, H. J.; Kruijtzer, J. A.; Liskamp, R. M. Characterization and activity of an immobilized antimicrobial peptide containing bactericidal PEG-hydrogel. *Biomacromolecules* **2014**, *15*, 3390−3395.

(76) Robinson, D. A.; Griffith, R. W.; Shechtman, D.; Evans, R. B.; Conzemius, M. G. In vitro antibacterial properties of magnesium metal against *Escherichia coli*, *Pseudomonas aeruginosa* and *Staphylococcus aureus*. *Acta Biomater.* **2010**, *6*, 1869−1877.

(77) Sawai, J.; Ishizu, N.; Itoh, M. Kinetic analysis of the bactericidal action of magnesium oxide powder slurry against *Escherichia coli*. *Biocontrol Sci.* **2003**, *8*, 123−127.

(78) Aničić, N.; Vukomanović, M.; Koklič, T.; Suvorov, D. Fewer Defects in the Surface Slows the Hydrolysis Rate, Decreases the ROS Generation Potential, and Improves the Non-ROS Antimicrobial Activity of MgO. *Small* **2018**, *14*, No. 1800205.

(79) Ribeiro, M.; Monteiro, F. J.; Ferraz, M. P. Infection of orthopedic implants with emphasis on bacterial adhesion process and techniques used in studying bacterial-material interactions. *Biomatter* **2012**, *2*, 176−194.

(80) Dizaj, S. M.; Lotfipour, F.; Barzegar-Jalali, M.; Zarrintan, M. H.; Adibkia, K. Antimicrobial activity of the metals and metal oxide nanoparticles. *Mater. Sci. Eng., C* **2014**, *44*, 278−284.

(81) Das, B.; Moumita, S.; Ghosh, S.; Khan, M. I.; Indira, D.; Jayabalan, R.; Tripathy, S. K.; Mishra, A.; Balasubramanian, P. Biosynthesis of magnesium oxide (MgO) nanoflakes by using leaf extract of Bauhinia purpurea and evaluation of its antibacterial property against *Staphylococcus aureus*. *Mater. Sci. Eng., C* **2018**, *91*, 436−444.

(82) Clements, M. O.; Watson, S. P.; Foster, S. J. Characterization of the major superoxide dismutase of *Staphylococcus aureus* and its role in starvation survival, stress resistance, and pathogenicity. *J. Bacteriol.* **1999**, *181*, 3898−3903.

(83) Karavolos, M. H.; Horsburgh, M. J.; Ingham, E.; Foster, S. J. Role and regulation of the superoxide dismutases of *Staphylococcus aureus*. *Microbiology* **2003**, *149*, 2749−2758.

(84) Abdal Dayem, A.; Hossain, M. K.; Lee, S. B.; Kim, K.; Saha, S. K.; Yang, G.-M.; Choi, H. Y.; Cho, S.-G. The role of reactive oxygen species (ROS) in the biological activities of metallic nanoparticles. *Int. J. Mol. Sci.* **2017**, *18*, No. 120.

(85) Nel, A.; Xia, T.; Mädler, L.; Li, N. Toxic potential of materials at the nanolevel. *Science* **2006**, *311*, 622−627.

(86) Fu, P. P.; Xia, Q.; Hwang, H.-M.; Ray, P. C.; Yu, H. Mechanisms of nanotoxicity: generation of reactive oxygen species. *J. Food Drug Anal.* **2014**, *22*, 64−75.

(87) Reading, N. C.; Sperandio, V. Quorum sensing: the many languages of bacteria. *FEMS Microbiol. Lett.* **2006**, *254*, 1−11.

(88) Sifri, C. D. Quorum sensing: bacteria talk sense. *Clin. Infect. Dis.* **2008**, *47*, 1070−1076.

(89) Czárán, T.; Hoekstra, R. F. Microbial communication, cooperation and cheating: quorum sensing drives the evolution of cooperation in bacteria. *PLoS One* **2009**, *4*, No. e6655.

(90) MacKintosh, E. E.; Patel, J. D.; Marchant, R. E.; Anderson, J. M. Effects of biomaterial surface chemistry on the adhesion and biofilm formation of *Staphylococcus epidermidis* in vitro. *J. Biomed. Mater. Res., Part A* **2006**, *78*, 836−842.

(91) Andrade, J.; Hlady, V. Protein Adsorption and Materials Biocompatibility: A Tutorial Review and Suggested Hypotheses. *Biopolymers/Non-Exclusion HPLC*; Springer: New York, 1986; pp 1−63.

(92) Wilson, C. J.; Clegg, R. E.; Leavesley, D. I.; Pearcy, M. J. Mediation of biomaterial−cell interactions by adsorbed proteins: a review. *Tissue Eng.* **2005**, *11*, 1−18.

(93) Jiang, W.; Tian, Q.; Vuong, T.; Shashaty, M.; Gopez, C.; Sanders, T.; Liu, H. Comparison study on four biodegradable polymer coatings for controlling magnesium degradation and human endothelial cell adhesion and spreading. *ACS Biomater. Sci. Eng.* **2017**, *3*, 936−950.

(94) Necula, B. S.; van Leeuwen, J. P. T. M.; Fratila-Apachitei, L. E.; Zaat, S. A. J.; Apachitei, I.; Duszczyk, J. In vitro cytotoxicity evaluation of porous TiO_2−Ag antibacterial coatings for human fetal osteoblasts. *Acta Biomater.* **2012**, *8*, 4191−4197.

(95) Schofield, W.; Badyal, J. A substrate-independent approach for bactericidal surfaces. *ACS Appl. Mater. Interfaces* **2009**, *1*, 2763−2767.

(96) Francolini, I.; Donelli, G. Prevention and control of biofilm-based medical-device-related infections. *FEMS Immunol. Med. Microbiol.* **2010**, *59*, 227−238.